Holographic Interferometry Study of an Axisymmetric Shock-Wave/Boundary-Layer Strong Interaction Flow

S. E. Dunagan* and J. L. Brown†
NASA Ames Research Center, Moffett Field, California
and
J. B. Miles‡
University of Missouri, Columbia, Missouri

An experimental study has been conducted of the axisymmetric shock-wave/turbulent boundary-layer strong interaction flow generated in the vicinity of a cylinder-cone intersection. The present data are useful in the documentation and understanding of compressible, turbulent strong-interaction flows and are part of a more general effort to improve turbulence modeling for compressible, two- and three-dimensional strong viscous/inviscid interactions. The nominal freestream Mach number is 2.85, with a maximum Reynolds number of 18×10^6 based on model length. Three cone angles (12.5, 20, and 30 deg) were studied, giving negligible, incipient, and large-scale flow separation, respectively. A primary emphasis in this paper is on the application of the holographic interferometry technique to these flow cases. The density field is deduced from an interferometric analysis based on the Abel transform. Supporting data are obtained using a two-dimensional laser velocimeter. The attached flow case is observed to be steady, whereas the separated cases exhibit shock unsteadiness. Comparisons with Navier-Stokes computations using a two-equation turbulence model are presented. The study illustrates the utility of holographic interferometry for detailed instantaneous flowfield characterization and provides data useful in the evaluation of computational schemes.

Introduction

COMPRESSIBLE turbulent strong viscous/inviscid interactions, such as shock-wave/boundary-layer[1,2] and expansion-fan/boundary-layer[3] interactions, often dominate in establishing the flowfield over supersonic aerodynamic bodies. These interactions can involve considerable upstream influence, as well as significant streamwise- and normal-pressure gradients. Navier-Stokes computational methods[4,5] with a suitable turbulence model most accurately represent the physics of these flows. However, shock unsteadiness related to the turbulence field occurs when the flow separates, and these computational methods do not presently include such transients. Additionally, the boundary-layer turbulence field may include nonequilibrium effects[6,7] not incorporated in the more widely used turbulence models. A more comprehensive understanding of these interactions is required for accurate predictive flow and turbulence modeling to be achieved.

With the current emphasis on the development of computational techniques for aerodynamic design and analysis, an essential requirement is the extensive documentation of experimental flows for the validation of computational methods. Documentation of supersonic strong interactions is complicated by the sensitivity of these flows to disturbances such as pressure or hot-wire probes and undesired end-wall three-dimensionality. Should flow reversal occur, use of pressure and hot-wire probes is invalid. Flowfield documentation of compressible strong interactions may be accomplished,

however, with nonintrusive methods such as laser velocimetry and holographic interferometry.[8,9] Within inviscid flow regions, laser velocimetry and holographic interferometry provide a redundant measurement capability, since the velocity and density fields are directly related. Within viscous flow regions, these two laser flowfield diagnostic techniques provide a complementary measurement capability useful in understanding these compressible viscous mechanisms.

This paper describes an experimental study of the axisymmetric shock-wave/turbulent boundary-layer strong interaction flow generated in the vicinity of a cylinder-cone intersection. A subsequent cone-afterbody intersection generated an axisymmetric expansion-fan/turbulent-boundary-layer interaction, which is also presented. The mean flowfield characteristics of these strong interactions are emphasized, with a primary reliance on the nonintrusive holographic interferometry measurement technique. Oil flow, wall pressure, and laser velocimeter (LV) measurements are included to augment interferometric data. Three cone angles representing attached (12.5 deg), incipient separation (20 deg), and fully separated (30 deg) flow were considered. The current experimental study was conducted as part of a more general program to improve flow and turbulence modeling of compressible two- and three-dimensional interactions.

Navier-Stokes computations are included in this paper (with only minimal attention to computational details) and illustrate the utility of interferometric data in code performance assessment. Mean flow data (shock position, density, and velocity fields) obtained from holographic interferometry and laser velocimetry methods are compared with Navier-Stokes computations.

Experimental Description

Flow and Model Geometry

Experiments were conducted in the High Reynolds Number Channel I at Ames Research Center. A two-dimensional Mach 3 nozzle was used to establish supersonic flow in the 24.5-cm-wide × 38.1-cm-high test section. The model shown in Fig. 1

    *Aerospace Engineer.
    †Research Scientist.
    ‡Professor of Mechanical Engineering.

Fig. 1 Model configuration in wind tunnel.

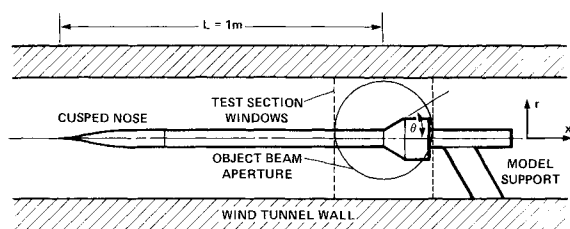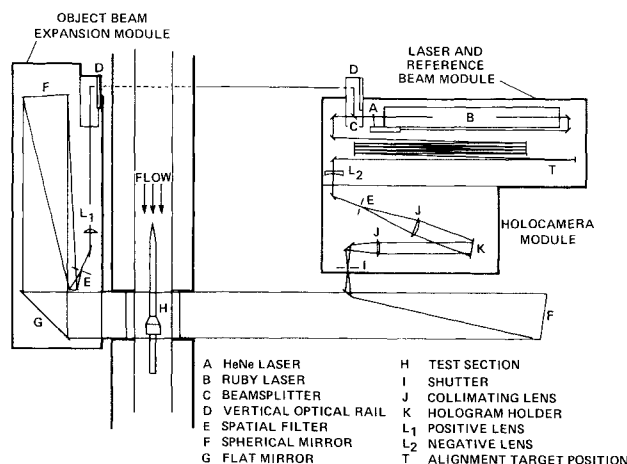| A | HeNe LASER | H | TEST SECTION |
B	RUBY LASER	I	SHUTTER
C	BEAMSPLITTER	J	COLLIMATING LENS
D	VERTICAL OPTICAL RAIL	K	HOLOGRAM HOLDER
E	SPATIAL FILTER	L_1	POSITIVE LENS
F	SPHERICAL MIRROR	L_2	NEGATIVE LENS
G	FLAT MIRROR	T	ALIGNMENT TARGET POSITION

Fig. 2 Interferometer layout for hologram construction.

consists of a 5.08-cm-diam cylinder with interchangeable conic flare and afterbody attachments. The cusped nose of the cylinder was designed to suppress shock waves emanating from the model tip and thus enhance flow uniformity in the interaction region. Cone angles for the interchangeable flares were chosen to provide flows with negligible, incipient, and large-scale separation. Several models with various angles were examined experimentally, and values of 12.5, 20, and 30 deg were selected. Afterbody diameters were chosen to place the expansion corner at a distance of 6 cm (along the model surface) from the cylinder-cone intersection so that the expansion would occur at a uniform location in the nonequilibrium boundary layer downstream of the interaction.

A total pressure P_t of 1.7 atm was selected to be compatible with the refractive index requirements of the interferometer. Measured wall pressures indicated an average Mach number M_∞ of 2.85. An average total temperature of 270 K was measured. The corresponding unit Reynolds number is 18×10^6/m. The initial boundary-layer thickness just upstream of the compression corner is 1.1 cm. Oil-flow measurements were made to confirm flow symmetry and to identify the extent of the separated region.

Shock-wave unsteadiness was observed in high-speed shadowgraph data for axisymmetric flows with large cone angles, particularly in the region of the separation shock. The unsteadiness complicates the comparison of interferometric data, which are essentially instantaneous, with LV and wall pressure data, which are time-averaged. However, for the three cone angle models reported here, shock unsteadiness was significant for only the 30-deg model flow. An averaging of several instantaneous interferometric data sets was employed to obtain mean flow data for the unsteady case.

Holographic Interferometer

The holographic interferometer designed and constructed for use in this study is shown in Fig. 2. Optical elements

were mounted to three aluminum base plate modules with heavy aluminum rods. These modules were, in turn, attached to the tunnel infrastructure to provide an economical, reasonably vibration-resistant instrument.

A Q-switched ruby laser provided illumination. A 5-mW helium-neon laser mounted to the ruby laser rail provided a reference beam for alignment of both the ruby cavity and the downbeam optics. The ruby laser generated pulses of approximately 20-ns duration at $\lambda = 694.3$ nm wavelength. The output was split with 30% reflectance into the object beam. This beam was transmitted under the wind tunnel and onto the object beam expansion module, where it was spatially filtered and collimated at a 30.48-cm working diameter.

Following passage through the test section, the object beam was focused through an electronic shutter and recollimated onto the hologram. The reference beam was multiply reflected on the laser module to match the object beam path length within the coherence length of the laser. A beam intensity adjustment lens L_2 was used prior to spatial filtering, beam expansion, and collimation at the hologram. Photographic plates were used to record simple absorption holograms. The object and reference beams intersected at an angle of 20 deg, with the hologram inclined equally to each beam. The laser and holocamera modules were bolted together and shared a common support platform. This configuration minimized beam wander and permitted spatial filtering of the reference beam 15.24 m downbeam from the laser. The spatial filtering of both beams far downbeam ensured good beam quality.

Interferometric Data Reduction

In this study, interferograms were formed from the reconstruction of an undisturbed (flow-off) object wave that had traversed a test section of uniform refractive index interfered with a perturbed (flow-on) wave that traversed the refractive index field on the flow. The flow-on wave contained information on the refractive index integrated along its path. If no path length variations had been introduced by vibration or deliberate plate misalignment, the interferogram resulting from the reconstruction process would exhibit infinite-fringe spacing in regions of constant refractive index and would be referred to as an "infinite-fringe" interferogram. If such is not the case, the interferogram is labeled "finite-fringe." For infinite-fringe interferograms, the spatial distribution of fringe number $N(x,y)$, referenced to a zero value at a point in the field where the refractive index n_0 is known, is given by the expression

$$N(x,y) = \frac{1}{\lambda} \int_{z_1}^{z_2} [n(x,y,z) - n_0] \, dz \qquad (1)$$

If the refractive index field is a function of radius, integral inversion may be accomplished by the use of Abel transform methods. Classical numerical Abel transform methods[10] calculated an unrealistic overshoot in the shock region of the current axisymmetric flow. To avoid this numerical problem, a least-squares Abel transform algorithm was originated for this study. First, and consistent with prior Abel inversion techniques, a higher-order orthogonal polynomial series curve was fit to raw fringe number data $N(y_k)$ from the model surface to the freestream along profiles of constant x. One problem arises since the polynomials used cannot describe the fringe number variation in the vicinity of the shock wave where $\partial N/\partial y$ becomes infinite. However, strong refraction effects within 1 mm of the shock caused a gap in valid data for this region. Thus a parabolic fit, $N^2 \propto (y - y_{shock})$, between the outermost valid data and the shock was used to fill this region. To enhance Abel transform performance over the critical elements adjacent to the shock, fringe number values were approximated with even spacing in fringe number and uneven spacing in y.
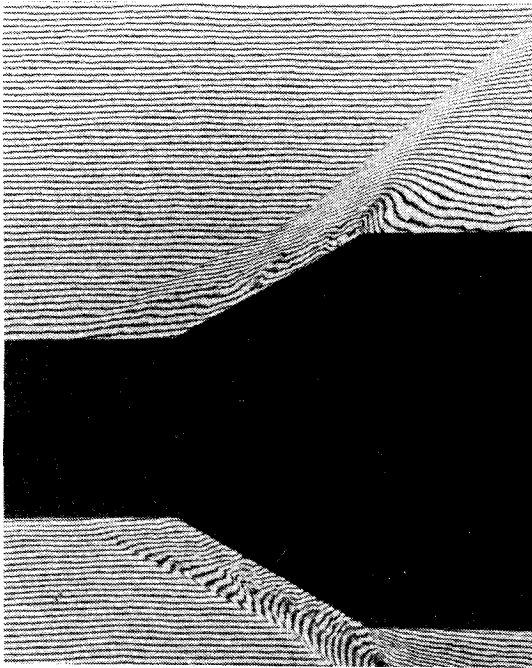
Fig. 3 Horizontal finite-fringe reconstruction for 30-deg model $(M_\infty = 2.85, Re_L = 18 \times 10^6)$.
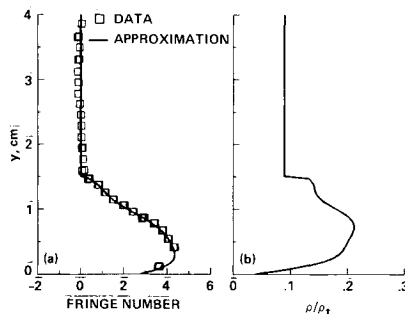

Fig. 4 Profile at $x = 2$ cm, 30-deg model, $Re_L = 18 \times 10^6$: a) fringe number; b) density.

This curve-fit procedure generated a smoothed approximation to the fringe number data at unevenly spaced locations $\tilde{N}(y_i)$. An Abel transform inversion to solve for index of refraction was required next. Previous Abel inversion algorithms, however, could not easily accommodate the uneven data spacing requirements of the resultant curve-fit data just obtained. To meet these needs, a least-squares method of Abel transform inversion was originated for this study. In this procedure, the index of refraction is assumed to be composed of the sum of a finite series:

$$n(r) = \sum_i a_i f_i(r)$$

where

$$f_i = 1 \quad \text{if } r \in [r_i, r_{i+1}]$$
$$= 0 \quad \text{otherwise}$$

Then, for an axisymmetric phase object, the fringe number is

$$\tilde{N}(y_j) = \sum_i a_i F_i(y_j) \qquad (2)$$

where

$$F_i(y_j) = \int_{y_j}^{r_{i+1}} f_i(r) \cdot (r^2 - y_j^2)^{-\frac{1}{2}} r \, dr \quad \text{if } y_j < r_{i+1}$$

$$= 0 \qquad\qquad\qquad \text{if } y_j \geq r_{i+1}$$

A least-squares analysis is then applied to Eq. (2), resulting in a system of equations to be solved for the a_i coefficients. A symmetric matrix results which is easily inverted by Gaussian elimination.

Having approximated the radial fringe number variation, and then transformed profiles via the least-squares Abel method, density may be deduced by means of the simple relation:

$$n = 1 + K\rho \qquad (3)$$

where the Gladstone-Dale constant K is a property of the gas. This relation permits the calculation of density profiles at any desired location.

Laser Velocimeter

As this investigation represented the initial application of the particular holographic interferometer described previously, it was desirable to provide complementary experimental velocity data to permit an evaluation of interferometry system performance. The laser velocimetry system employed in the present study has been previously used and reported.[7] This LV system is a two-dimensional, two-color, forward-scatter system using 0.5 μm polystyrene particles as scattering centers. The fringe patterns of the two channels were oriented at ± 45 deg to the tunnel axis with the 40-MHz Bragg-shifted fringes moving downstream. Typically, 35,328 individual velocity measurements were acquired at each location.

Computations

Computations were performed by C. C. Horstman using methods outlined in Ref. 4. The partial-differential equations used to describe the mean flowfield are the time-dependent, Reynolds-averaged, Navier-Stokes equations for axisymmetric flow of a compression fluid. For turbulence closure, the two-equation k-ϵ turbulence model[11] was used. The numerical procedure used is the basic explicit second-order, predictor-corrector finite-difference method of Mac-Cormack, modified by an efficient implicit alogorithm.[12] The computational domain extended in the flow direction from -5 to 8 cm (referenced to an origin at the cone-cylinder intersection) and in the vertical direction from the model surface to 9 cm. A 65×45 mesh was employed with constant mesh spacing in the streamwise direction. Radial mesh point spacing was small ($y_1^+ \approx 1$) in the boundary layer, increasing logarithmically with distance from the model surface. The upstream boundary conditions were obtained from a boundary-layer solution that matched the experimentally determined velocity profile, Mach number, and total pressure.

Results and Discussion

Interferogram Analysis and Flow Visualization

A sample interferogram for the 30-deg model is shown in Fig. 3, which represents a finite-fringe interferogram reconstructed using the dual-plate method. The spatial resolution of this interferometric data, as limited by optical aberration and digitization error, was determined to be on the order of 1 mm. This interferogram gives a clear view of the shock wave and separation zone geometries, as well as the relative strengths of density gradients in the flow. A great deal of information may be obtained from a simple visual inspection of this raw data.
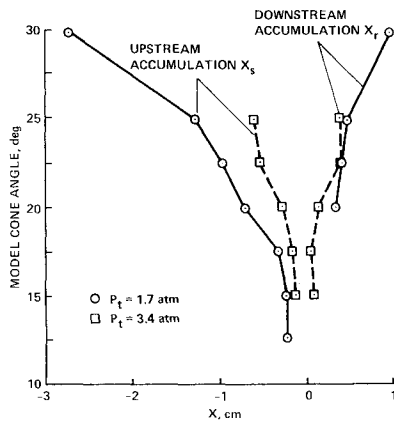
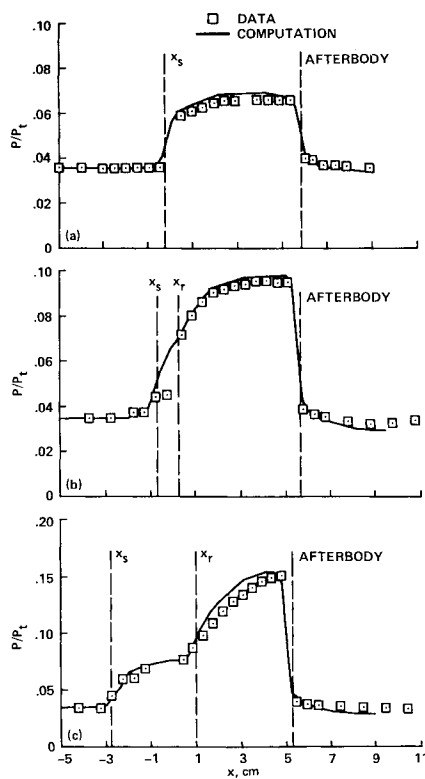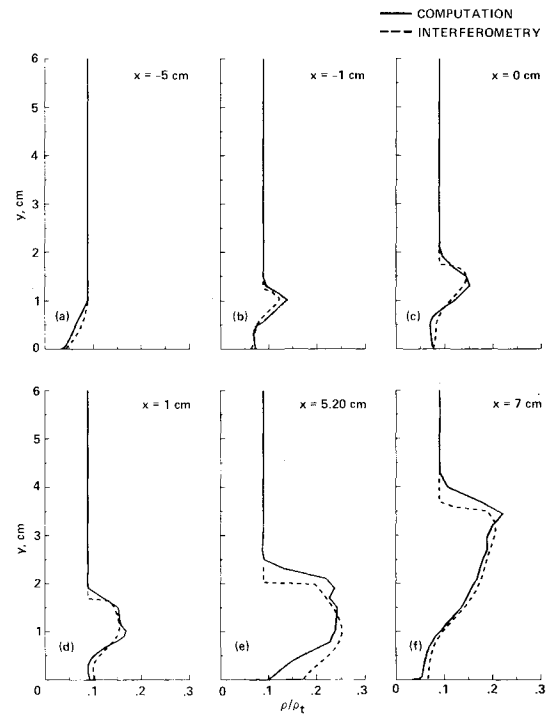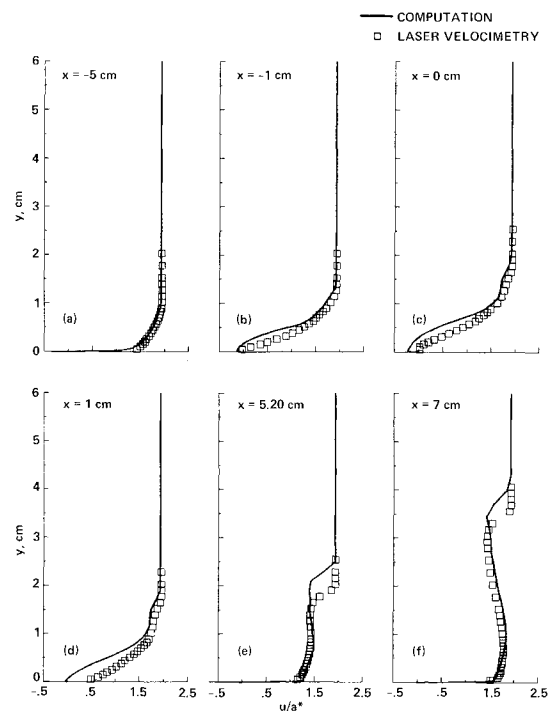Fig. 5 Oil-flow point of accumulation.

Fig. 7 Density profiles for 30-deg model ($Re_L = 18 \times 10^6$).

Fig. 6 Experimental and calculated surface pressure distributions: a) 12.5-deg model; b) 20-deg model; c) 30-deg model.

Fig. 8 Velocity profiles for 30-deg model ($Re_L = 18 \times 10^6$).

The horizontal finite-fringe reconstruction of Fig. 3 is preferred to infinite-fringe reconstruction for quantitative data reduction. Inversion of the refractive index integral of Eq. (1) by Abel transform techniques is most accurate if fringe number data are approximated at a large number of closely spaced radial positions. Finite-fringe reconstruction greatly increases the number of fringe-profile intersections, increasing the spatial resolution of the data and reducing data approximation errors. This finite-fringe reconstruction effectively superimposes a linear $\Phi(y)$ fringe number function over the field of view. Since $\partial r/\partial y$ is positive above the model and negative below, the superposition yields the nonsymmetrical fringe pattern of Fig. 3. The $\Phi(y)$ function may be calculated from fringe spacing in the freestream where the density is known to be uniform. Equation (1) now becomes

$$N(x,y) - \Phi(y) = \frac{1}{\lambda} \int [n(x,y,z) - n_0]\, dz \qquad (4)$$

and may be inverted using the numerical Abel transform technique.

A close examination of interferogram data reveals a nonuniformity in fringes located in the boundary layer downstream of the compression corner for the 30-deg model. This fringe distortion is thought to be associated with large-scale boundary-layer turbulence downstream of the interaction region. Such instantaneous turbulence is inherently three-dimensional. Nevertheless, the linearity of the Abel transform operator permits an accurate evaluation of the mean flow from an ensemble average of random samples for

this ergodic process. Mean densities reported herein were obtained from an average of eight interferograms for the 30-deg model and four interferograms for the 12.5- and 20-deg models. The evaluation of a larger sample would increase confidence in the accuracy of these mean values.

Figure 4a shows raw and least-squares approximated fringe number data along a profile located 2 cm downstream of the compression corner for the 30-deg cone model. The density profile of Fig. 4b was obtained by applying the least-squares Abel transform technique to Fig. 4a fringe number data. The presence of a weak reattachment shock system is indicated by the slight change in curvature observed at a y location of 1.2 cm.

Flowfield Data

In the present experiment, as the cone angle increases from 12.5 to 30 deg, the shock strength increases, the shock position moves upstream, and the boundary layer separates. Figure 5 presents a summary of an oil-flow study which illustrates this process. Oil applied at the surface in a compresssion corner shock-wave/boundary-layer interaction tends to accumulate at one of two locations, x_s being an oil accumulation upstream of the corner, and x_r being an oil accumulation downstream of the corner. Interpretation of the x_s and x_r oil accumulations as points of separation and reattachment can only be approximate.

For cone angles less than 20 deg, no downstream x_r accumulation was observed, suggesting that the constant upstream x_s accumulations were associated with shock formation rather than separation. For cone angles of 20 deg and greater, increasing distance between x_s and x_r accumulations is indicative of the expected increase in separation bubble size with the stronger shock.

Surface pressure distributions from pressure data and the computation are presented in Fig. 6 for the three cone angles. Oil-flow accumulation points x_s and x_r are indicated. Shock and expansion fan locations are clearly indentified by pressure jumps. Weakening of the shock by the boundary layer is manifest by a more gradual pressure rise. In the 20-deg pressure data, a small constant surface pressure region is observed corresponding to the separated region indicated by the oil flow. This plateau is not present in the computation. Beyond this detail, good agreement is observed between pressure data and computed pressure distributions.

Velocity profiles from LV and computation, and density profiles from interferometry and computation for the 12.5-deg model were compared. Overall agreement between computation and experiment in both density and velocity profiles is quite good. Because of past experience, a great deal of faith may be placed in the capability of the Navier-Stokes solver to accurately predict this weaker interaction flow. Furthermore, the well-established confidence in the LV system as a reliable research tool lends credibility to the quality of the acquired LV data. Therefore, the main result of this comparison for this flow condition is to establish the validity of the interferometric technique in the analysis of these flows. This is done directly by comparison with the computation as well as indirectly, insofar as the physical models within the computation are accurate, by comparison with LV data.

Density profiles from interferometry and computation, and velocity profiles from LV and computation at six streamwise locations for the 30-deg model at 1.7 atm are presented in Figs. 7 and 8. In this case, the strong interaction and large separated zone reduce confidence in the computed values. An assessment of code performance is possible with evaluation against both interferometer and LV data. An overprediction of the radial extent of separation in the calculation is apparent in the velocity profiles of Figs. 8b and 8c. Computed density profiles show a somewhat thicker region of nearly constant density close to the wall (as compared to interferometry profiles) at these locations, but this

comparison is not nearly as informative as that of the velocity profiles.

The interferometric density profile of Fig. 7d is in the region of highest shock unsteadiness and exhibits a smoothing of shock structure detail owing to averaging over several interferograms. The single interferogram density profile of Fig. 4b, also at an x location of 2 cm, shows good agreement with the computed density profile of Fig. 8d on density peak and wall values and on the relative location of the reattachment shock system, but shows the entire density field to be shifted inward. This indicates an inboard shock position for the particular interferogram of Fig. 4b compared to the average shock position.

The computed density profile located at the cone-afterbody corner shows strong disagreement with interferometry data (see Fig. 7e). Interferometry data in this region were subject to a slight degree of fringe dropout very near the model surface but in general were quite reliable. Fluid in this region had traversed an extensive region of nonequilibrium boundary layer. The cause of the discrepancy may be related to turbulence modeling detail in this nonequilibrium region, but such a statement may not be made conclusively within the scope of the present investigation. No such disagreement is observed in the comparison of velocity profiles.

Velocity profiles do, however, give evidence of an outboard overprediction of shock location by the computation for profiles at x locations of 5.20 and 7.0 cm. This error is confirmed in the density comparison, although the more obvious grid resolution limit would tend to soften the magnitude of the mislocation. It may be seen that both interferometric and LV data are quite useful in the assessment of code performance for this flow, and that benefits are realized through the use of both experimental techniques together.
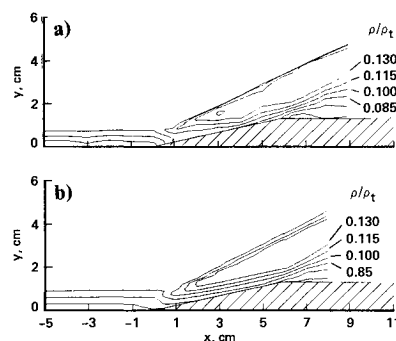

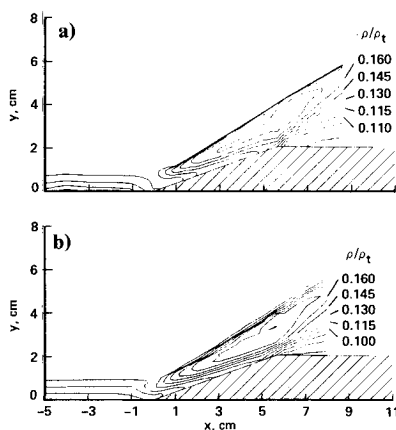Fig. 9 Density contours for 12.5-deg model: a) interferometer; b) computation.

Fig. 10 Density contours for 20-deg model: a) interferometer; b) computation.
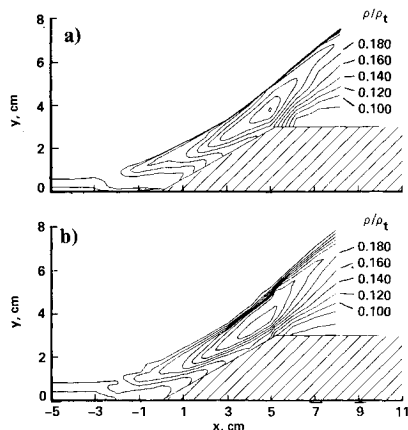
Fig. 11 Density contours for 30-deg model: a) interferometer; b) computation.

Experimental density contour plots for the three models are presented in Figs. 9–11 to provide thorough documentation of the flow. Contour plots of the computed densities are included for comparison. Reattachment shock detail is present in interferometric and computational density contours for the 30-deg model. In the absence of large-scale separation, the bifurcated shock does not appear in the 12.5- and 20-deg cases. A comparison of density contours from interferometric data and computation re-emphasizes the slight outboard displacement and broadening of the shock provided by the calculation. Density levels compare well over the entire field.

Concluding Remarks

To provide quantitative aerodynamic data for comparison with computational and predictive schemes, an experimental study has been conducted for an axisymmetric shock-wave/turbulent-boundary-layer strong-interaction in the vicinity of a cylinder-cone intersection. Primary experimental emphasis has been on the application of holographic interferometry for density field measurement, with laser velocimeter data included to supplement interferometric techniques. The explicit second-order, predictor-corrector finite-difference method of MacCormack with the two-equation k-ϵ turbulence model has been applied, and the obtained solution has been shown to compare favorably with interferometric and laser velocimeter data.

In a departure from what has generally been reported in the literature, the computation overpredicts the extent of separation. Nevertheless, surface pressure data and computed values show good agreement. Interferometry and LV data agree on shock location, whereas the computation places the shock slightly outboard. The results presented herein are useful in the documentation and understanding of strong viscous-inviscid interactions and confirm the utility of holographic interferometry techniques for supersonic, axisymmetric flowfield analysis.

References

[1]Settles, G. S., Fitzpatrick, T. J., and Bogdonoff, S. M., "Detailed Study of Attached and Separated Compression Corner Flow Fields in High Reynolds Number Supersonic Flow," *AIAA Journal,* Vol. 17, June 1975, pp. 573–585.

[2]Ardonceau, P. L., "The Structure of Turbulence in a Supersonic Shock Wave/Boundary-Layer Interaction," *AIAA Journal,* Vol. 22, Sept. 1984, pp. 1254–1262.

[3]Dussauge, J. P. and Gaviglio, J., "Turbulent Boundary-Layer/Expansion Interaction at Supersonic Speed," Inst. de Mechanique Statistique de le Turbulence, Univ. de Aix-Marseille II, Travaux de l'I.M.S.T. LA, No. 130 au CNRS Contracts ONERA, June 1980.

[4]Horstman, C. C. and Johnson, D. A., "Prediction of Transonic Separated Flows," *AIAA Journal,* Vol. 22, July 1984, pp. 1001–1003.

[5]Coakley, T. J., "Turbulence Modeling Methods for the Compressible Navier-Stokes Equations," AIAA Paper 83-1958, July 1983.

[6]Johnson, D. A. and King, L. S., "A New Turbulence Closure Model for Boundary Layer Flows with Strong Pressure Gradients and Separation," AIAA Paper 84-0175, Jan. 1984.

[7]Brown, J. L. and Viswanath, P. R., "An Experimental Study of a Supercritical Airfoil," AIAA Paper 84-2187, Aug. 1984.

[8]Johnson, D. A., Bachalo, W. D., and Owen, F. K., "Transonic Flow Past a Symmetric Airfoil at High Angle of Attack," *Journal of Aircraft,* Vol. 18, Jan. 1981, pp. 7–14.

[9]Delerey, J. M., "Investigation of Strong Shock Turbulent Boundary Layer Interaction in 2-D Transonic Flows with Emphasis on Turbulence Phenomena," AIAA Paper 81-1245, June 1981.

[10]Vest, C. M., *Holographic Interferometry,* Wiley, New York, 1979.

[11]Jones, W. P. and Launder, B. E., "The Prediction of Laminarization with a Two-Equation Model of Turbulence," *International Journal of Heat and Mass Transfer,* Vol. 15, Feb. 1972, pp. 301–314.

[12]MacCormack, R. W., "A Numerical Method for Solving the Equations of Compressible Viscous Flow," *AIAA Journal,* Vol. 20, Sept. 1982, pp. 1275–1281.